Materials and Design 92 (2016) 888–896

Contents lists available at ScienceDirect

Materials and Design

journal homepage: www.elsevier.com/locate/matdes

# Effect of microstructure on corrosion behavior of a Zr–Sn–Nb–Fe–Cu–O alloy

Liangyu Chen [a,e], Qifeng Zeng [b], Jiuxiao Li [a], Junqiang Lu [b], Yao Zhang [a], Lai-Chang Zhang [c], Xujuan Qin [a], Weijie Lu [a,*], Lefu Zhang [d], Liqiang Wang [a,*], Di Zhang [a]

[a] State Key Laboratory of Metal Matrix Composites, Shanghai Jiao Tong University, Shanghai 200240, China
[b] Nuclear Engineering Research and Design Institute, Shanghai 200233, China
[c] School of Engineering, Edith Cowan University, 270 Joondalup Drive, Joondalup, Perth, WA 6027, Australia
[d] School of Nuclear Science and Engineering, Shanghai Jiao Tong University, Shanghai 200240, China
[e] School of Mathematics and Science, Jiangsu University of Science and Technology, Zhenjiang, Jiangsu 212003, China

ARTICLE INFO

*Article history:*
Received 22 July 2015
Received in revised form 11 November 2015
Accepted 14 December 2015
Available online 15 December 2015

*Keywords:*
Zirconium
Microstructure
Corrosion kinetics
Undulation
Tensile property
Second phase particle

ABSTRACT

This work investigates the effect of microstructure on tensile properties and corrosion behavior of a Zr–Sn–Nb–Fe–Cu–O alloy. Scanning electron microscope, transmission electron microscope, electron back scattering diffraction, tensile tests and autoclave corrosion test were jointly carried out to characterize in detail the microstructural features and properties of the alloy studied. The corrosion rate constant increases with decreasing the degree of recrystallization. The sample with slower evolution of undulated interface exhibits higher tensile strength and possesses better corrosion resistance. The plasticity of sample can hardly be the rigorous limitation on corrosion performance, which is attributed to the consistent consummation of the deformed substrate around the interface during corrosion to make the inner undeformed substrate become fresh interface. Furthermore, second phase particles (SPPs) may play a role in the nucleation of cracks in the oxide.



## 1. Introduction

Zirconium alloys have been widely used as cladding material in nuclear reactors. In order to reach higher burnups, the corrosion resistance of fuel claddings has been considered as one of the most important properties to control the performance and the safety of nuclear reactors [1–5]. Generally, corrosion behavior initially takes place at the oxide/metal interface, which is mainly obedient to parabolic law [6,7]. A thin black oxide film strongly bonded to the metal is formed at the initial stage of corrosion. Once the oxide has reached a few microns in thickness (pre-transition), an acceleration of corrosion kinetics is observed (post-transition), followed by a second cycle of parabolic growth rates [7]. The transition time is the important assessment criteria to evaluate the corrosion resistance of zirconium alloys. When transition occurs, large cracks connected in the oxide and the oxide splits into two layers [6]. It is suggested that the oxide layers are associated with the number of transitions during corrosion [8]. The thickness of fully developed oxide is related to corrosion kinetics, which has been well established on layered oxides [8,9]. The oxide growth and transformation that occur at the metal/oxide interface produce large volume dilation [10]. This dilation is accompanied with large compressive stress in the oxide and large tensile stress in the metal that induce undulated interface [10]. Parise et al. [11] performed a modeling to analyze stress distribution in the oxide with undulated interface and indicated that tensile stress is located above the wavy crests of undulations perpendicular to the interface. Vermaak et al. [10] found that the stress increased with increasing the amplitude of undulations. If the stress was high enough, a crack would be triggered in the oxide [10,12].

It is reported that the corrosion behavior is very sensitive to the microstructure of alloys, which would be tailored by different sample processing such as deformation and heat treatment [13–19]. A number of recent work has been implemented to correlate the microstructure of zirconium alloys with their corrosion behavior [13–18]. Ly et al. [13] found that the corrosion kinetics transition of stress relieved and recovered samples took place earlier than that of recrystallized ones and the corrosion resistance of recrystallized samples monotonously increased with the reduction in grain size. Furthermore, it is also suggested that a "soft" substrate could release the in-plane stress via creep [13], thereby decreasing the stress in the oxide. However, Likhanskii et al. [14] used the method of elastic energy minimization to evaluate the transition parameters. Their results showed that the alloy with higher tensile strength and higher plasticity could resist the formation of undulations in the oxide/metal interface, and hence postponing the transition. The variation of heat treatment conditions, especially final annealing, would result in a corresponding change in the microstructure of the processed samples. Park et al. [15,16] found that HANA-4, HANA-6 and Zr–1.1Sn–0.2Nb–0.35Fe–0.15Cr–0.1Cu (in wt.%) alloys with lower

* Corresponding authors.
*E-mail addresses:* luweijie@sjtu.edu.cn (W. Lu), wang_liqiang@sjtu.edu.cn (L. Wang).

http://dx.doi.org/10.1016/j.matdes.2015.12.067
0264-1275/

final annealing temperature had better corrosion resistance. Nevertheless, Ni et al. [17] observed that the ZIRLO alloy with different final heat treatments demonstrated very similar oxidation kinetics, which was in agreement with the results obtained in Zircaloy-4 alloy [18].

In the present work, Zr–Sn–Nb–Fe–Cu–O alloy samples with various microstructural features were elaborated to investigate the correlation among microstructure, tensile properties and corrosion behavior. Two of them had a similar microstructure, with the aim to examine the susceptibility of microstructure to corrosion performance. Another one had a substantially different microstructure from the former ones, dedicating to study the influence of microstructure on corrosion behavior. Autoclave corrosion tests were conducted up to 200 days. Weight gain changes were observed as the measure of corrosion resistance. Meanwhile, the microstructural features including grain size, degree of recrystallization, amount of second phase particles (SPPs), oxide cross-sectional microstructure, oxide fracture and tensile properties were characterized in detail. This work aimed to enhance the understanding of the corrosion mechanism and to correlate the microstructure and corrosion behavior.

## 2. Material and methods

### 2.1. Samples preparation

Zr–Sn–Nb–Fe–Cu–O alloy was prepared by vacuum arc re-melting for three times to obtain chemical homogeneity. The alloy contains 0.55% Sn, 0.32% Fe, 0.35% Nb, 0.05% Cu, and 0.079% O and with Zr as the balance (in wt.%), where the contents of Sn, Fe, Nb and Cu were analyzed by inductively coupled plasma atomic emission spectrometry and the content of O was determined by Nitrogen/Oxygen Exterminator (TC600, LECO Corporation). The disk-shape ingot was 110 mm in diameter and 50 mm in height. After forged at 1000 °C, the height of ingots was reduced to 10 mm and then the ingots were β-quenched at 1050 °C. Fig. 1 illustrates the schedules of the processing (e.g. low temperature pre-deformation and rolling) and heat treatments after β-quenching. The low temperature pre-deformation in procedure 2# was rolled at 470 °C with a reduction of 40% in height, which can result in refinement of grains [20]. Alloying elements would dissolve into matrix after the second β-quenching since β-Zr has a larger solid solubility than α-Zr [21]. Low temperature annealing can slow down the recrystallization of alloys. As such, different microstructure of samples can be elaborated. All the samples were labeled corresponding to their processing schedules (e.g. the sample 1# stood for the sample which was processed from the procedure 1#, and so on).

### 2.2. Microstructure analysis

Microstructures were characterized using a FEI Sirion 200 field emission gun scanning electron microscope (SEM) and a JEOL-2100F transmission electron microscope (TEM) equipped with an energy dispersive X-ray spectroscopy (EDS) detector with an accelerated voltage of 200 kV. Samples for SEM observations were polished according to standard metallographic techniques and then etched in the solution containing $H_2O$:$HNO_3$:HF of 9:9:2 (in vol.%). Specimens for TEM observations were prepared using a twin-jet polishing with a solution ($C_2H_5OH$:$HClO_4$ = 9:1 in vol.%) at a voltage of 20 V and a temperature of −30 °C. In order to obtain the oxide cross-section fracture surface, the corroded samples were etched in the solution for 15 min to dissolve the metal substrates. Then, the oxide films extruding the metal substrates were gently fractured using a tweezer. The cross-sectional oxides and their fracture surface were coated with a gold film to improve the electrical conductivity before SEM observation.

Electron back scattering diffraction (EBSD) measurements were carried out with an AZtec HKL Max system, installed on a NOVA NanoSEM 230 scanning electron microscope. Samples prepared for EBSD measurements were polished by colloidal silica after etching. EBSD patterns were analyzed by the channel 5 software. The grain boundary angle condition used to define a grain was fixed to 10°. The channel 5 software can also identify the degree of recrystallization via comparing the collected crystallographic data with the existing data in database.

### 2.3. Corrosion test

Samples used for autoclave corrosion testing were 15 mm × 20 mm in size and chemically polished using a pickling solution ($H_2O$:$HNO_3$:$H_2SO_4$:HF = 3:3:3:1 in vol.%) at 30–50 °C and finally cleaned by deionized water. The corrosion resistance of the sample was evaluated by measuring their weight gain per unit surface area in relation to the exposure time (i.e. 3, 7, 14, 42, 70, 100, 130, 160, and 200 days). The corroded samples were named after their procedure number and exposure time (e.g. sample 1#-100 stands for the sample 1# after 100 days exposure, and so on). According to the ASTM-G2/88 (Standard Test Method for Corrosion Testing of Products of Zirconium, Hafnium, and Their Alloys in Water at 680 °F or in Steam at 750 °F) [22], corrosion tests were conducted with a static isothermal autoclave in 0.01 mol/L LiOH aqueous solution at 360 °C under a saturation pressure of 18.6 MPa.

### 2.4. Tensile tests

Tensile tests were performed using a Zwick Z100/SN3A universal testing machine at both room temperature and 380 °C. Dog-bone flat tensile samples with a nominal gauge length of 15 mm and a cross-section of 12 mm × 0.6 mm were cut by electric discharge machining from the final samples parallel to the rolling direction. The samples were subsequently mechanically ground with 2000 grit SiC paper. A displacement rate of 1 mm/min was used for all the tensile tests.

## 3. Results

### 3.1. General microstructural characteristics

Fig. 2 reveals EBSD inverse pole figure (IPF) maps for samples 1#, 2# and 3# which have partial recrystallized microstructures due to relatively low final annealing temperature. As seen from Fig. 2a and b, samples 1# and 2# have a similar microstructural morphology except for discrepant average grain size (i.e. 1.2 μm for sample 1# and 0.7 μm for sample 2#). It could be found that adding pre-deformation into conventional fabrication process substantially refines the grains as reported in Ref. [23] and our previous study [20]. The sample 3# presents an inhomogeneous microstructure with lots of grains in irregular shape (Fig. 2c). The average grain size is 1.5 μm, just slightly larger than that of samples 1# and 2#. The EBSD results reveal that the degrees of recrystallization of samples 1# and 2# are about 50% and 60%, respectively. Sample 3# exhibits large grains in association with small grains. The size of certain grains in samples 3# is even greater than 10 μm. The maximum grain size reaches 12.1 μm (Fig. 2c). It should be noted that second β-quenching was performed on samples 3#. The grains were coarsened at this step and were flatten by cold rolling afterward. However, because of relatively "low" intermediate annealing temperature (470 °C) and final annealing temperature (470 °C) after the second β-quenching, recrystallization is very sluggish in sample 3#. The degree of recrystallization of sample 3# is only about 2%, indicating recrystallization has just begun. Thus grains in irregular shape and deformed microstructure are still presented.

Fig. 3 represents the features of SPPs in the experimental alloys. The SPPs distribute randomly within the grains and along the grain boundaries in samples 1# and 2# (Fig. 3a and b). Similar distributions of SPPs have been found in commercial zirconium alloys [24,25]. The average size of SPPs is about 71 ± 5 nm and 68 ± 5 nm for samples 1# and 2#, respectively. None of precipitates is found in sample 3# but remnant laths and shattered grains (Fig. 3c). Lath structures are observed by SEM

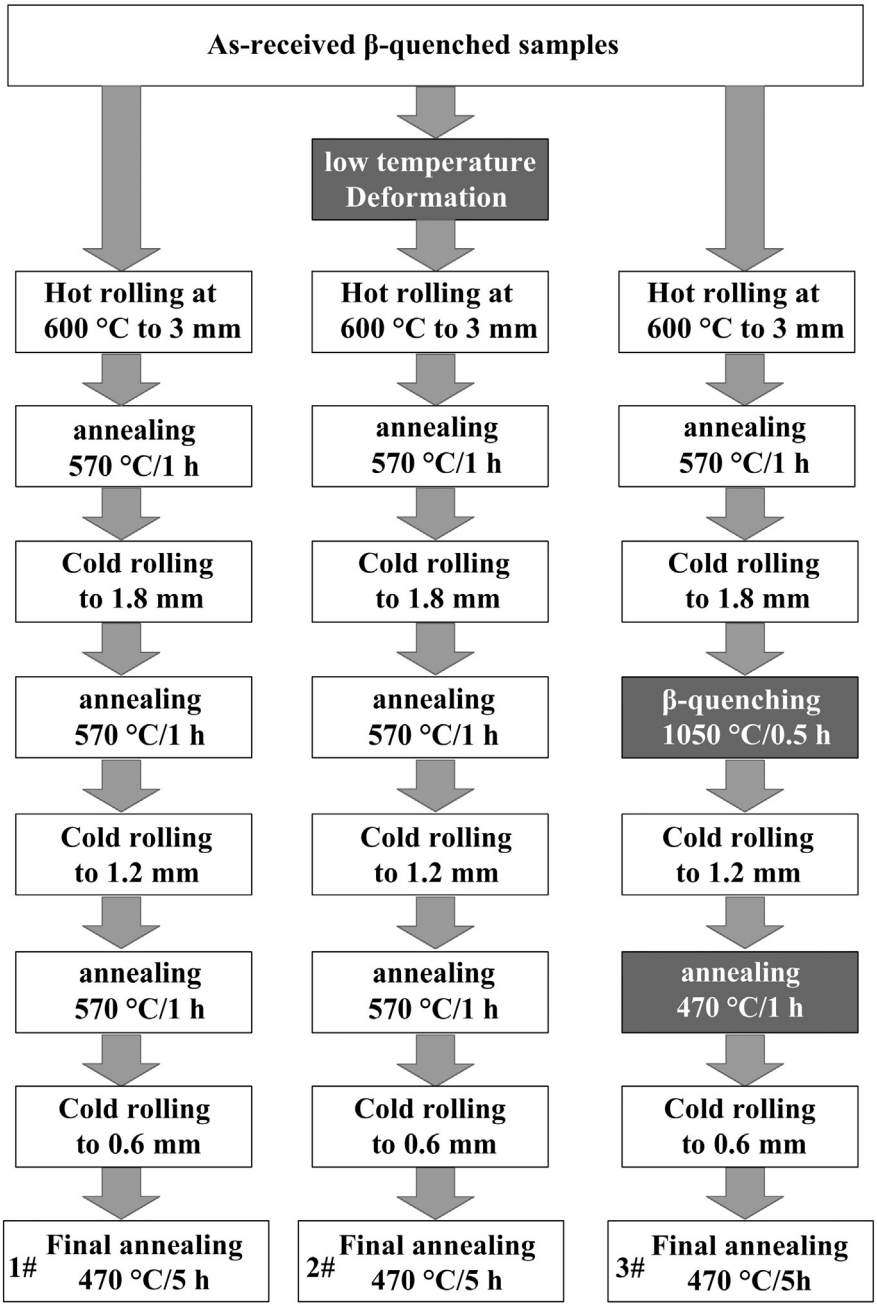


**Fig. 1.** Process flow of experimental alloy. Samples were obtained by three kinds of processing procedure.

but not detected by EBSD, which may be owing to the difference in magnification and principle of imaging between the two techniques [20]. SPPs dissolve into matrix after the second β-quenching since β-Zr has a larger solid solubility than α-Zr [21]. The temperature of heat treatment for sample 3# after the second β-quenching is relatively low, which might be the main reason accounting for the disappearance of SPPs in sample 3#. Fig. 3d, e and f present the TEM images for the samples studied. The SPPs in samples 1# and 2# are in spherical or ellipsoidal shape and distributed randomly (Fig. 3d and e). The intermetallic $(Zr,Nb,Cu)_2Fe$-type precipitates are found in both groups and have face-centered cubic (FCC) structure (the insets of Fig. 3d and e). The chemical compositions of SPPs obtained by EDS attached on TEM are 2.0–6.9% Nb, 21.6–23.7% Fe, 3.5–5.9% Cu (in wt.%) and the balance is Zr. Large number of remnant laths with high density dislocations are observed in sample 3# (Fig. 3f), which were produced by the second β-quenching and still presented after final annealing [26]. These findings agree well with the results of EBSD and SEM for sample 3# (Figs. 2c and 3c).

### 3.2. Strength and plasticity

Fig. 4 shows the stress–strain curves for all samples at room temperature and 380 °C. The ultimate tensile strength of sample 1# is about 380 MPa at room temperature and 181 MPa at 380 °C, respectively. The percent elongation of sample 1# is about 31.7% at room temperature and 36.2% at 380 °C, respectively. Both ultimate tensile strength and percent elongation of sample 2# are 400 MPa and 32.5% at room temperature and 201 MPa and 37.1% at 380 °C, respectively, which are slightly greater than the corresponding ones for sample 1#. Due to the samples have a partial recrystallization state, it is difficult to build quantitative relation between microstructural parameters and strength according to Hall–Petch relation. Furthermore, refined crystalline

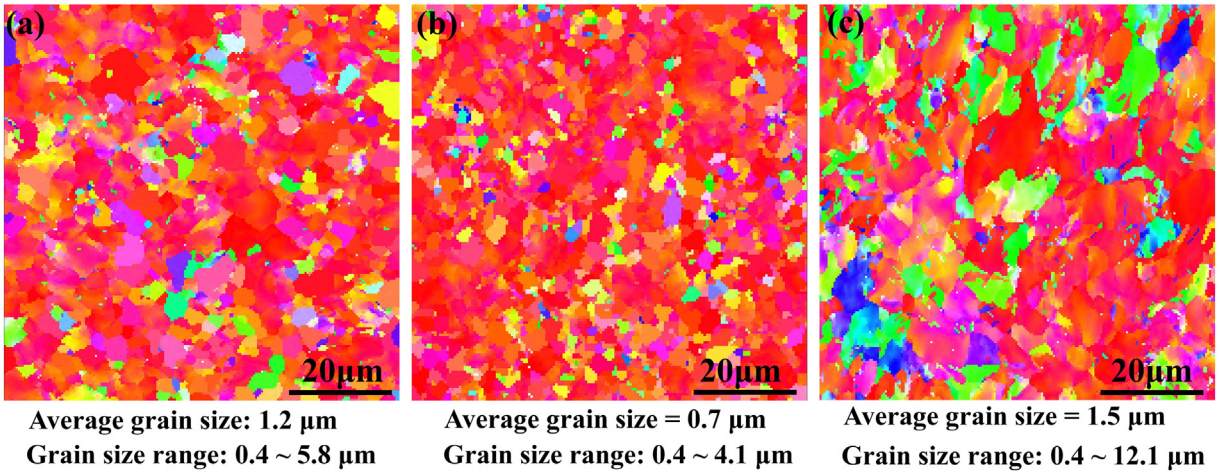


**Fig. 2.** EBSD inverse pole figure maps and grain size for (a) sample 1#, (b) sample 2# and (c) sample 3#. Samples have partial recrystallized microstructures due to relatively low final annealing temperature. The grain boundary angle condition used to define a grain was fixed to 10°.

strengthening can enhance the strength and plasticity of alloys simultaneously [27]. Therefore, the enhancements in mechanical properties of sample 2# in comparison to sample 1# should be attributed to the finer grains in sample 2# than in sample 1#. The sample 3# shows a large increase in ultimate tensile strength (590 MPa) along with a decrease in elongation (14.5%) at room temperature, which results from its low degree of recrystallization. At 380 °C, the tensile strength of sample 3# decreases to 381 MPa but it is still much higher than those of samples 1# and 2#. However, the percent elongation of sample 3# is 22.5% at 380 °C, which is exceeding 1.5 times that at room temperature. It has been reported that recrystallization kinetic would be affected by applying stress for zirconium alloy when aging at relatively low temperatures [28]. A high applied stress (exceeding 100 MPa) accelerates the nucleation rate thus promoting recrystallization [28]. This mechanism might be responsible for the large incremental percent elongation of sample 3# at 380 °C in comparison with that at room temperature.

### 3.3. Corrosion behavior

#### 3.3.1. Weight gain

Fig. 5 shows the corrosion weight gain of samples as a function of exposure time after the autoclave tests in 0.01 mol/L LiOH aqueous

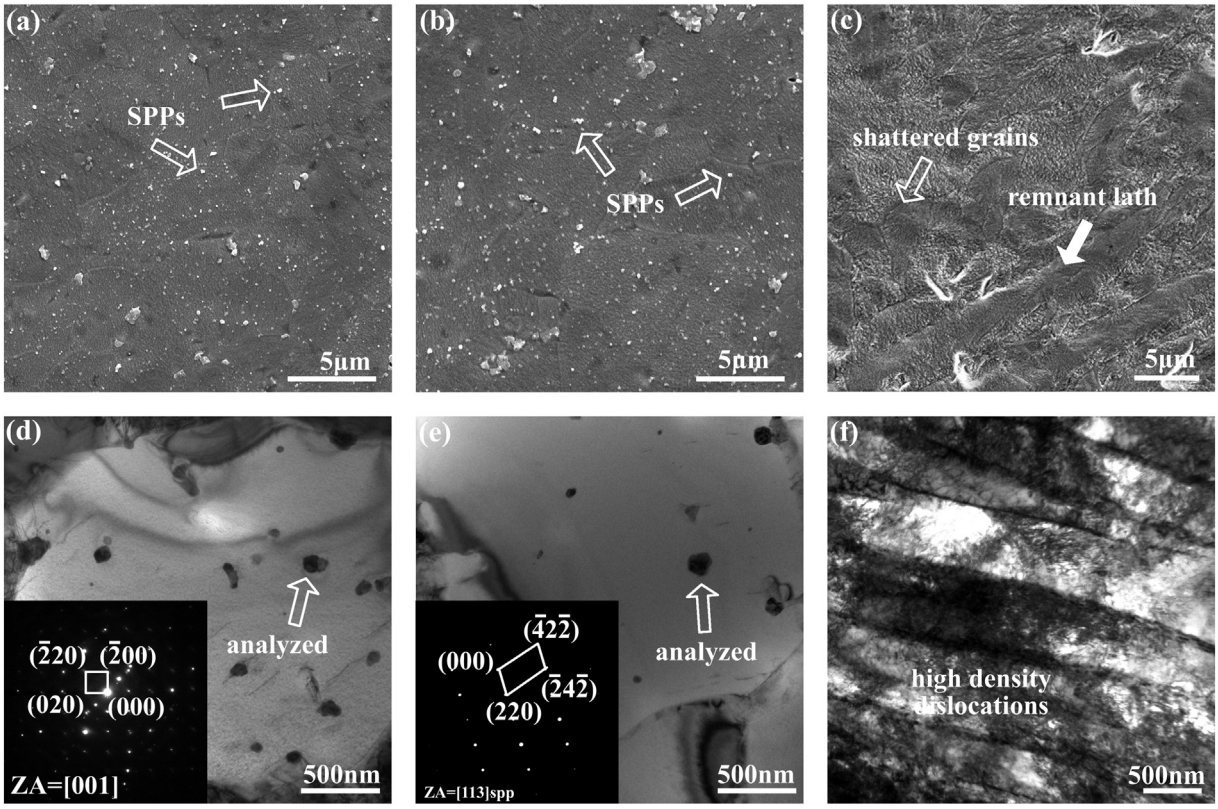


**Fig. 3.** SEM and TEM images for (a) and (d) sample 1#, (b) and (e) sample 2# and (c) and (f) sample 3# after final annealing. The SPPs distribute randomly within the grains and along the grain boundaries in samples 1# and 2#. None of precipitates is found in sample 3# but remnant laths and shattered grains. The insets are the SADPs of SPPs which are indicated by white hollow arrows in (d) and (e).

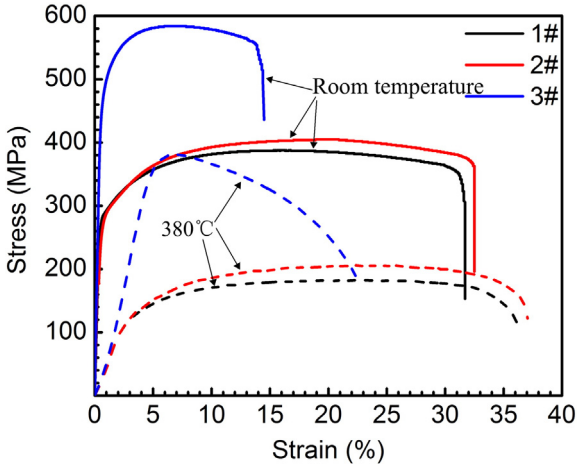


**Fig. 4.** Stress–strain curves for all samples at room temperature and 380 °C. Sample 3# shows a large increase in ultimate tensile strength with a decrease in elongation compared to samples 1# and 2#.

solution at 360 °C/18.6 MPa. Both sample 1# and sample 2# exhibit typical corrosion kinetics with an indication of change from pre- to post-transition after 100 days. With up to 200 days, sample 3# shows no apparent sign of a transition in corrosion kinetics. The corrosion resistance depends significantly on the corrosion transition point. Higher corrosion resistance is invariably related to a longer pre-transition period [29]. This assertion means that sample 3# has corrosion resistance superior to samples 1# and 2#.

It is important to mention that weight gain measurements are not sensitive enough to show the real time when the transition occurs. As shown in Fig. 5, it could be merely deemed that the transition phenomenon of samples 1# and 2# occurs between 100 days exposure and 130 days exposure. The weight gains of samples 1# and 2# are almost same before transition. After 100 days, distinct weight gains of samples 1# and 2# are observed. If the transition point is virtually identical, the difference in weight gains after transition between samples 1# and 2# would be almost the same as the one before transition [8,9]. However, the difference in weight gains between samples 1# and 2# is becoming larger after transition. Since the weight gain of zirconium alloys mainly

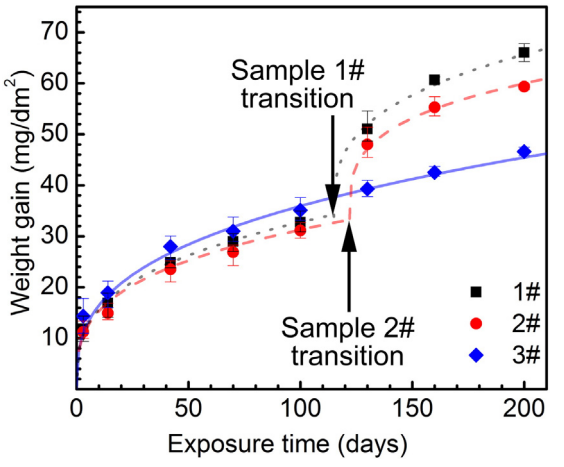


**Fig. 5.** Autoclave corrosion weight gain profile for all samples after 200 days. Both samples 1# and 2# show a post-transition phenomenon after 100 days. However, with up to 200 days, sample 3# shows no apparent sign of a transition in corrosion kinetics.

obeys parabolic law, the corrosion rate constant can be measured by the following equation [30]:

$$w = kt^n \tag{1}$$

where $w$ is the weight gain, $k$ is a constant, $t$ is exposure time and $n$ is corrosion rate constant. According to the periodic corrosion kinetics of zirconium alloys [8], the transition time could be estimated (Fig. 5). The transition time of sample 2# (122 days) is longer than that of sample 1# (115 days). The estimated transition time is merely a calculated value to represent the corrosion resistance of samples, but not in reality. Some researchers proposed that the transition phenomenon did not take place suddenly, but during a short period [17,29]. This assumption was proposed according to the propagation of cracks in the oxide. To link the microstructures, tensile properties and corrosion behavior. Table 1 summarizes the grain size, SPPs size, volume fraction of SPPs, degree of recrystallization, tensile properties, estimated transition time and corrosion rate constant for all samples. As shown in Table 1, it is not possible to find a monotonous relation between some microstructural parameters and transition time, or between percent elongation and transition time. However, it seems that the corrosion resistance is enhanced with increasing the tensile strength and the corrosion rate constant increases with the decrease in degree of recrystallization. These findings demonstrate that corrosion behavior is sensitive to the microstructural alteration. To better understand the correlation among microstructures, tensile properties and corrosion behavior, the oxide microstructure in the samples studied was investigated.

### 3.3.2. Cross-sectional microstructures of oxide

SEM examinations showed that cracks parallel to the oxide/metal interface appear at transition point, which is commonly observed in Refs. [6,13,31,32]. Fig. 6 presents the cross-sectional microstructure of the oxide at 100 days and 160 days. For samples 1#-100 and 2#-100, a few cracks can be observed at the top of oxide/metal interface as indicated by red arrows in Fig. 6a and b. Ni et al. [17] suggested that such cracks play an important role as obstacles in impeding oxygen diffusion, slowing down oxygen diffusion rate. This kind of cracks acts as short-circuits for diffusion paths, thus increasing the corrosion rate. According to the experimental results presented in this work, lateral cracks are not presented on the oxide of sample 3#-100 (Fig. 6c) which has the best corrosion resistance in all of these samples. The thickness of oxide of samples 1#-160 and 2#-160 augments obviously after transition (Fig. 6d and e). The lateral cracks have linked up and the oxide has split into two layers as our previous report [6]. It has also been reported that the number of oxide layers is associated with the number of transitions [8]. Therefore, the propagation of lateral cracks in the oxide is suggested to be a precursor of the transition [24]. The transition time is always extended for the sample which has postponing appearance of lateral cracks. As shown in Fig. 6f, only quite a few small cracks are observed in the oxide of sample 3#-160. The morphology of oxide

**Table 1**
Summary of microstructural features, tensile properties and corrosion performance of the processed Zr–Sn–Nb–Fe–Cu–O alloy samples. UTS indicates ultimate tensile strength, and RT means room temperature.

| Sample no. | 1# | 2# | 3# |
|---|---|---|---|
| Grain size (μm) | 1.2 | 0.7 | 1.5 |
| SPPs size (nm) | 71 ± 5 | 68 ± 5 | – |
| Volume fraction of SPPs (%) | 2 ± 0.05 | 2 ± 0.05 | – |
| Degree of recrystallization (%) | 50 ± 5 | 60 ± 5 | 2 ± 2 |
| UTS (MPa) (RT) | 379.7 ± 2.9 | 399.0 ± 3.7 | 590.3 ± 4.5 |
| Percent elongation (%) (RT) | 31.6 ± 1.1 | 32.5 ± 0.37 | 14.0 ± 1.5 |
| UTS (MPa) (380 °C) | 182.3 ± 5.0 | 202.7 ± 4.6 | 381.3 ± 5.3 |
| Percent elongation (%) (380 °C) | 36.3 ± 0.5 | 37 ± 0.45 | 22.4 ± 0.33 |
| Estimated transition time | 115 | 122 | >200 |
| Corrosion rate constant $n$ | 0.32 | 0.31 | 0.34 |

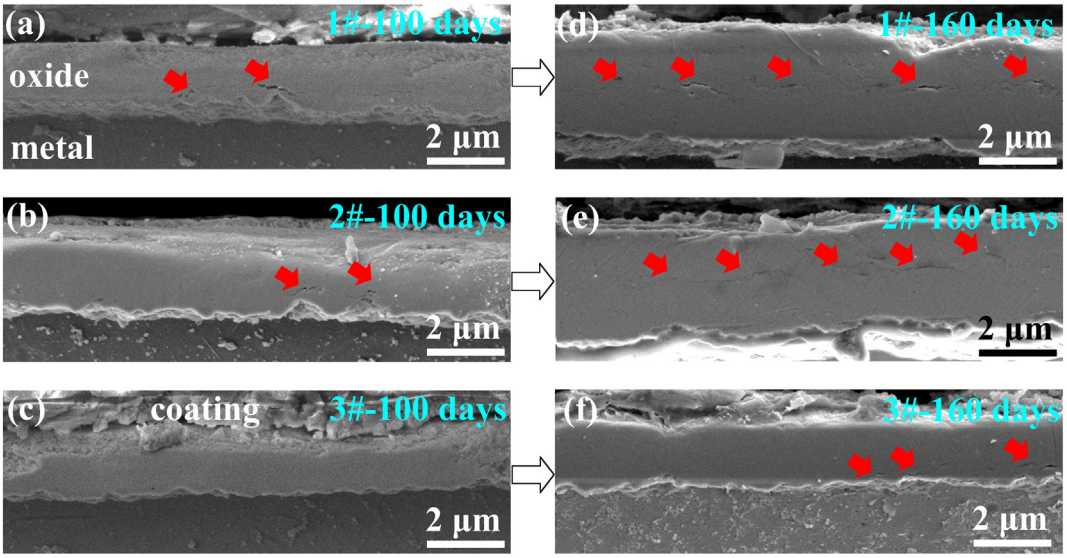


**Fig. 6.** Representative SEM micrographs of the oxide (cross-section): (a) sample 1#-100, (b) sample 2#-100, (c) sample 3#-100, (d) sample 1#-160, (e) sample 2#-160 and (f) sample 3#-160. More cracks are found in samples 1# and 2# compared to sample 3#.

cross-section also elucidates that the sample 3# has the best corrosion resistance.

The amplitude of undulations for samples is plotted versus time by collecting data from randomly choosing several SEM images, as shown in Fig. 7. For the post-transition samples (samples 1#-160 and 2#-160), only the cracks in the inner oxide layer are correlated to the amplitude of undulations [6]. One can note that the amplitude of undulations increases monotonously with the extending exposure time before transition. Furthermore, the cracks appear when the amplitude of undulation is sharp enough (Fig. 6a, b and f). The mild undulations would never trigger a crack in the oxide, such as the undulations in sample 3#-100 which has relatively low undulation amplitude (Fig. 6c). As the evolution of undulations, cracks are presented in sample 3#-160 (Figs. 6f and 7c). A simple conclusion could be drawn that the sample with slower evolution of undulations would have postponing transition and possess better corrosion resistance.

*3.3.3. Fractures of oxide*

Fig. 8 represents the fractures of oxide for samples 1#-160 and 3#-160. As seen from Fig. 8a, the oxide on sample 1#-160 become two layers, implying the corrosion kinetic transition of sample 1#-160 has occurred. The thickness of the fully developed layers in the oxide is about 1.6 μm. The sample 3#-160 is still in pre-transition. It could be simply regarded the lateral cracks as the first transition initiation cracks (Fig. 8b). The thickness of full developed oxide layer for sample 3#-160 is about 2 μm, which is rather thicker than that for sample 1#-160. Park et al. [15] reported that the fully developed oxide layer is 2.9 μm in HANA-6, 2.3 μm in HANA-4 and 2.2 μm in Zircaloy-4, which were corroded in primary water. The corresponding corrosion resistance ordered from high to low is HANA-6, HANA-4, Zircaloy-4. It is suggested that the thickness of the fully developed layer in the oxide is controlled primarily by the alloy composition regardless of the microstructures [15]. However, in the current work, it elucidates that the difference in thickness of fully developed oxide layers in the alloys is also associated with the difference in microstructures.

By comparing with the grain morphology of the oxide fractures of samples 1#-160 and 3#-160, it is found that more and larger columnar grains are presented in the oxide of sample 3#-160 than in the oxide of sample 1#-160. Oxide grows at an expense of metal substrate and SPPs are incorporated into oxide during corrosion [33,34]. SPPs are often considered as flaws in the oxide [6,24]. Tejland et al. [24] found that there are more lateral cracks presented in the Zircaloy-2 which has more SPPs and worse corrosion resistance. In this work, sample 1# contains a large number of SPPs. The grain morphology of the oxide for sample 1#-160 seems to be more flawed than that for sample 3#-160 (Fig. 8a). The flawed oxide is weaker and easier to form cracks than the oxide which maintains an intact columnar grain structure. It might be another possible reason for earlier appearance of lateral cracks in samples 1# and 2#.

## 4. Discussion

*4.1. The corrosion rate constant associated with the degree of recrystallization*

Initial oxide growth is governed by the inward diffusion of oxygen anions from zirconium bare surface into matrix inside [35]. None of oxide barrier exists between matrix and oxidants. Thus the weight gain increases rapidly at the initiation of corrosion as shown in Fig. 5. Furthermore, the diffusion rate of oxygen anions in defects (such as dislocations, grain boundaries) is much higher than that in bulk [36]. The unrecrystallized region usually consists of deformed structure or substructure which has more defects in matrix [37,38]. Thus, diffusion in unrecrystallized region would be faster than that in recrystallized region [38]. As seen from Fig. 2 and Table 1, after final annealing, samples have different degree of recrystallization which are about 50%, 60% and 2% for sample 1#, sample 2# and sample 3#, respectively. This discrepancy leads to various initial weight gain in samples. Although the weight gain of sample at the very beginning of corrosion is unknown, it still can be deduced by the first measure point of corrosion test. After 3 days exposure, the weight gains are 11.81 mg $dm^{-2}$, 11.23 mg $dm^{-2}$ and 14.36 mg $dm^{-2}$ for sample 1#-3, sample 2#-3 and sample 3#-3, respectively. The corresponding corrosion rate constants are 0.32, 0.31 and 0.34 before transition (Table 1). However, this slight difference in corrosion rate constant could not determine the corrosion resistance of samples, a very fast increase in weight gain always occurs when corrosion kinetic transition takes place.

*4.2. Transition phenomenon associated with mechanical properties*

The transition phenomenon is associated with lateral cracks in the oxide [6]. As shown in Figs. 6 and 7, lateral cracks never appear in the oxide with shallow undulations of interface. The sample with slower evolution of undulations of oxide interface would have delayed appearance of lateral cracks. In other words, the undulated interface is

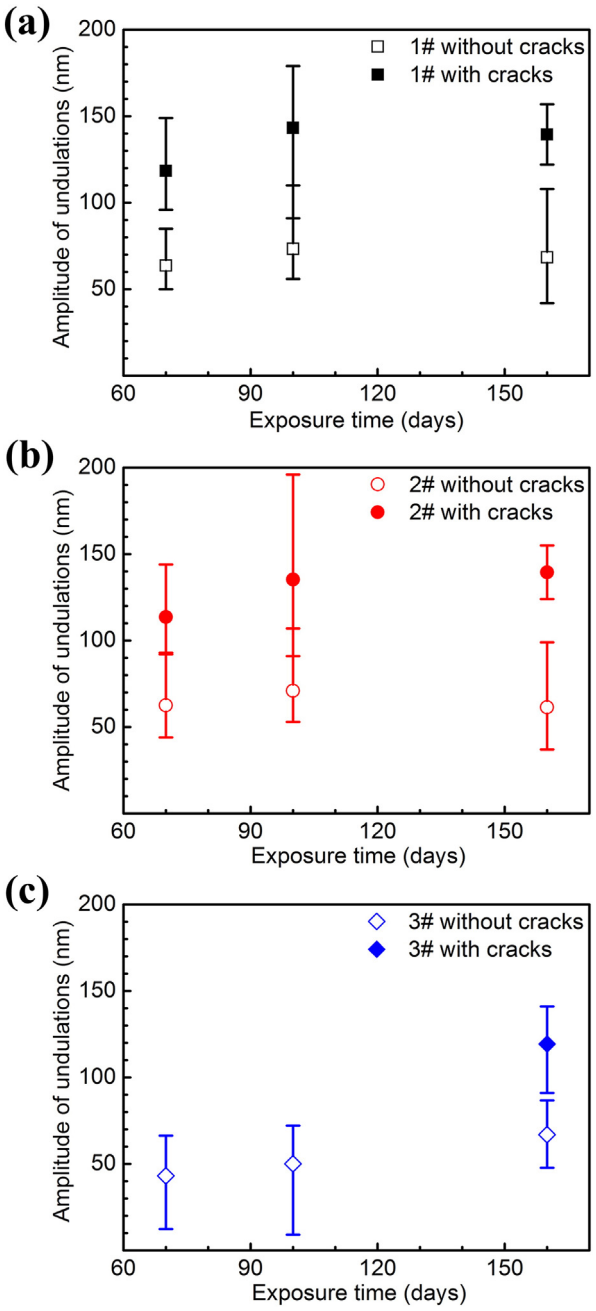


**Fig. 7.** Variation of the amplitude of undulations with/without cracks versus exposure time: (a) sample 1#, (b) sample 2# and (c) sample 3#. The amplitude of undulations increases monotonously with extending the exposure time before transition. The cracks appear when the amplitude of undulation is sharp enough.

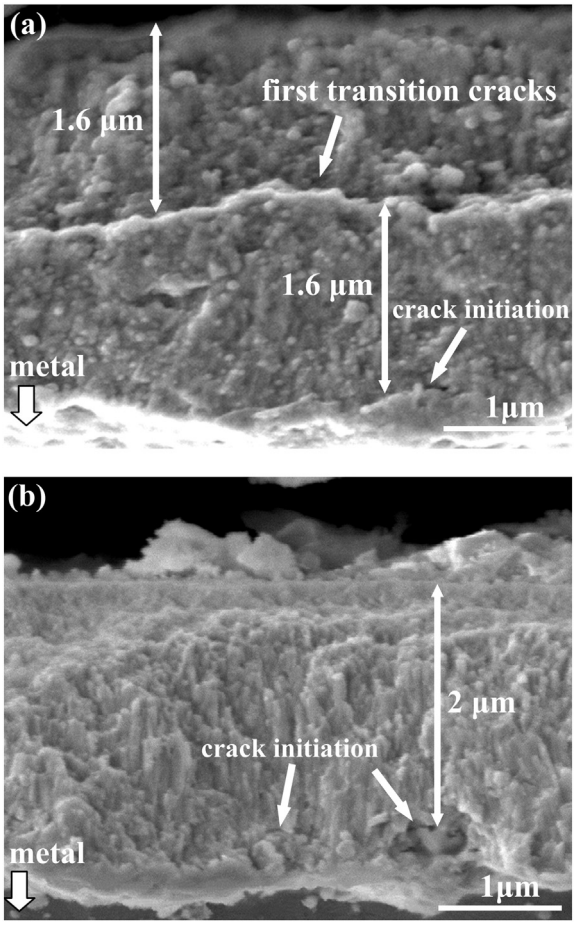


**Fig. 8.** Fracture surface of oxides formed on: (a) sample 1#-160 and (b) sample 3#-160. The thickness of the fully developed layers in the oxide is about 1.6 μm for sample 1# and 2 μm for sample 3#, respectively. The grain morphology of the oxide for sample 1#-160 seems to be flawed. More and larger columnar grains are presented in the oxide of sample 3#-160.

a prerequisite for formation of cracks in the oxide. Nevertheless, the evolution of undulations is still without consensus. Two hypotheses for evolution of undulation are by elastoplastic deformation [14,39] or by creep deformation [10,13]. In this work, sample 2# has a similar microstructure with sample 1#, whilst sample 2# with finer grains has higher tensile strength and higher plasticity compared to that of sample 1#. Correspondingly, sample 2# has a longer estimated transition time than sample 1#. This result agrees well with the results that the alloy with higher tensile strength and higher plasticity could possess better corrosion resistance [13,14]. However, sample 3# with the highest strength and the lowest plasticity has the best corrosion resistance. Therefore, it is found that the corrosion resistance of samples monotonously increases with the augment in strength regardless of plasticity (i.e. the elongation percentage). It indicates that the formation of undulations is more difficult if the metal has higher strength since more energy is needed, whilst the plasticity of sample may not be the rigorous limitation on corrosion resistance. Although sample 3# has the lowest plasticity among the three samples studied, its total elongation percentage reaches 22.4% at 380 °C (Table 1). The formation of undulations at the oxide/metal interface results from the deformation of local metal substrate. If the plasticity of alloy is too low, the metal substrate in the vicinity of the oxide/metal interface may crack or fracture during corrosion. As such, it is deduced that once the samples have adequate plasticity at working temperature, the corrosion performance is more likely to depend on the strength of alloys.

### 4.3. Deformation and consumption of local metal substrate

It should be pointed out that the oxide/metal interface moves toward the metal substrate during corrosion. The deformed metal substrate in the vicinity of interface is continuously consumed and transforms to oxide by inward diffusion of oxygen anions. Hence, the inner undeformed metal substrate becomes a fresh interface, and is then subjected to stress. That means the strain of local metal substrate would not be unlimited. The moving rate of the interface is not constant and is in proportion to the weight gain rate. The time of stress applied on local metal substrate is also different at various depths.

Therefore, a schematic illustration to outline a plausible corrosion mechanism of zirconium alloy is proposed and given in Fig. 9. As seen from Fig. 9, it is assumed that there are four time points of $t_0$, $t_1$, $t_2$ and $t_3$, which are associated with various corrosion state of sample during

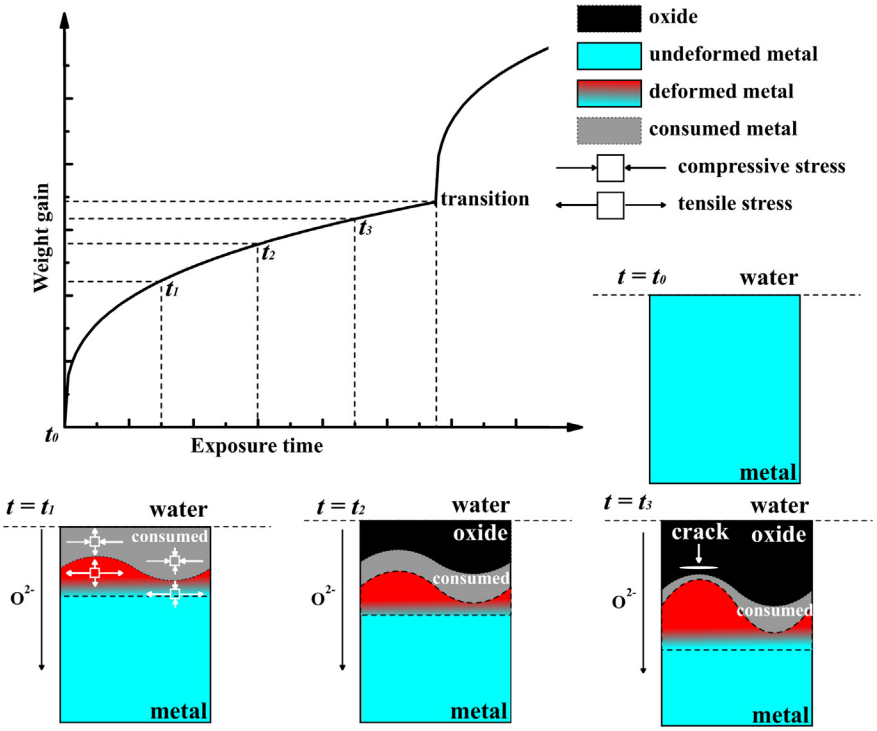


**Fig. 9.** Schematic illustration for the deformation of local metal substrate during corrosion. When the corrosion rate is high enough, the deformed metal is consumed before the undulations become sharp. None of cracks would be produced at the early stage of corrosion. The undulations become sharp due to the corrosion rate decreases as well as the movement of the oxide/metal interface. Once the metal substrate reaches a reasonable level of deformation, cracks are generated.

corrosion before corrosion kinetic transition. $t_0$ is defined as the initial state before sample has been corroded. At $t_0$, the bare zirconium surface directly contacts with corrosion environment. $t_1$ is defined as the early stage of corrosion. At $t_1$, part of zirconium is oxidized and undulated interface is presented. Due to the undulations, the metal substrate beneath the oxide is deformed. The distribution of stresses around the interface can be found elsewhere [11]. The corrosion rate is at a high speed at this stage since the weight gain is obedient to parabolic law (Fig. 5). As the results presented in the current work, the weight gains of samples 1# and 2# are respectively 11.80 mg $dm^{-2}$ and 11.22 mg $dm^{-2}$ after 3 days exposure, reaching one third of their weight gains after 100 days exposure. With the corrosion ongoing, the previously deformed layer is oxidized at $t_2$. The prior inner undeformed metal substrate becomes fresh interface and is deformed. At this stage, the corrosion rate is still at a relatively high speed, and the deformed metal is consumed before the undulations become sharp. However, as corrosion proceeds, the corrosion rate decreases. $t_3$ is close to the transition time. At $t_3$, the undulations become sharp due to the stress takes long time to act on the deformed region. Cracks are presented on the crests of sharp undulations. Parise et al. [11] calculated the stress distribution and proposed that in the case of oxide thickness was 2 μm (about 30 mg $dm^{-2}$) and the amplitude of undulations was 100 nm, the stress that affected region in substrate is about 400 nm in depth. The region where the stress exceeded 500 MPa was only about 140 nm in depth. As represented in Fig. 7, cracks are presented if the amplitude of undulations exceeds 100 nm. This result elucidates that once the metal substrate reaches a reasonable level of deformation, cracks are generated. After that the stress is relaxed by cracking [25]. Hence, the strain of metal substrate would not be unlimited. This is a good interpretation that the plasticity of sample can hardly be the rigorous limitation on corrosion transitions. Thus if the alloys with same chemical composition has adequate plasticity, the corrosion performance is more likely to depend on the strength of alloys. Therefore, sample 3# has the best corrosion resistance among the three samples studied and sample 2# has slightly better corrosion resistance than that sample 1#.

## 5. Conclusion

In this paper, the Zr–Sn–Nb–Fe–Cu–O alloy samples with different microstructures are obtained by three kinds of processing procedure. The correlation among microstructures, tensile properties and corrosion behavior have been investigated in detail. Some key conclusions can be drawn as follows:

(1) Transition time is the characteristic parameter of corrosion kinetics that is greatly sensitive to the microstructural alteration. For partial recrystallized samples, there is no simple correlation between transition time and some microstructural characteristics (grain size, elongation). The corrosion rate constant (0.32, 0.31 and 0.34 for samples 1#, 2# and 3#) increases with the decrease of degree of recrystallization (50%, 60%, 2% for samples 1#, 2# and 3#).
(2) The amplitude of undulations of the oxide/metal interface is affected by microstructural changes on the time scale of experiment. The lateral cracks presented above the crests of sharp undulations in the oxide are associated with the corrosion kinetics transition phenomenon. The sample with higher tensile strength has slower evolution of undulations and thus possesses better corrosion resistance.
(3) The corrosion resistance is improved with thickening the fully developed oxide layer. Meanwhile, second phase particles might play a role in the nucleation of cracks in the oxide, which results in poor-quality oxide.
(4) A schematic illustration is used to describe the deformation and consumption of local metal substrate. When the corrosion rate is high enough, the deformed metal is consumed before the undulations become sharp. None of cracks would be produced at the early stage of corrosion. The undulations become sharp due to the corrosion rate decreases with the movement of the oxide/metal interface. Once the metal substrate reaches a reasonable level of deformation, cracks are generated. Hence,

the plasticity of sample can hardly be the rigorous limitation on corrosion transitions.

(5) For their balanced performance, samples 1# and 2# can be used as structural materials (such as nozzle and grid) in the reactor. Sample 3# has excellent corrosion resistance but low plasticity. It can be utilized as fuel cladding candidate.

## Acknowledgments

The authors would like to acknowledge financial support provided by 973 Program under Grant No.: 2014CB046701, National Science Foundation under Grant No:51302168, New Teachers' Fund for Doctor Stations, Ministry of Education under Grant No: 20120073120007, Shanghai Pujiang Program under Grant No: 15PJD017 and Jiangxi Foreign Cooperation Program under Grant No.: 20144BDH80004. The authors also would like to acknowledge Instrumental Analysis Center of Shanghai Jiao Tong University for providing technology support.

## References

[1] M. Wen, H. Li, D. Yu, G. Chen, X. Chen, Uniaxial ratcheting behavior of Zircaloy-4 tubes at room temperature, Mater. Des. 46 (2013) 426–434.
[2] L. Chen, J. Li, Y. Zhang, L.C. Zhang, W. Lu, L. Zhang, et al., Zr–Sn–Nb–Fe–Si–O alloy for fuel cladding candidate: Processing, microstructure, corrosion resistance and tensile behavior, Corros. Sci. 100 (2015) 332–340.
[3] H. Chen, C. Long, T. Wei, W. Gao, H. Xiao, L. Chen, Effect of Ni interlayer on partial transient liquid phase bonding of Zr–Sn–Nb alloy and 304 stainless steel, Mater. Des. 60 (2014) 358–362.
[4] W. Tao, C. Cai, L. Li, Y. Chen, Y.L. Wang, Pulsed laser spot welding of intersection points for Zircaloy-4 spacer grid assembly, Mater. Des. 52 (2013) 487–494.
[5] H. Yang, J. Shen, Y. Matsukawa, Y. Satoh, S. Kano, Z. Zhao, et al., Effects of alloying elements (Sn, Nb, Cr, and Mo) on the microstructure and mechanical properties of zirconium alloys, J. Nucl. Sci. Technol. 52 (2015) 1162–1173.
[6] L. Chen, J. Li, Y. Zhang, L.C. Zhang, W. Lu, L. Zhang, et al., Effects of alloyed Si on the autoclave corrosion performance and periodic corrosion kinetics in Zr–Sn–Nb–Fe–O alloys, Corros. Sci. 100 (2015) 651–662.
[7] T. Arima, K. Miyata, Y. Inagaki, K. Idemitsu, Oxidation properties of Zr–Nb alloys at 500–600 °C under low oxygen potentials, Corros. Sci. 47 (2005) 435–446.
[8] A. Yilmazbayhan, A.T. Motta, R.J. Comstock, G.P. Sabol, B. Lai, Z. Cai, Structure of zirconium alloy oxides formed in pure water studied with synchrotron radiation and optical microscopy: relation to corrosion rate, J. Nucl. Mater. 324 (2004) 6–22.
[9] P. Bossis, D. Pecheur, L. Hanifi, J. Thomazet, M. Blat, Comparison of the high burn-up corrosion on M5 and low tin Zircaloy-4, zirconium in the nuclear industry: 14th international symposium, ASTM STP 1467 (2006) 494–525.
[10] N. Vermaak, G. Parry, R. Estevez, Y. Bréchet, New insight into crack formation during corrosion of zirconium-based metal-oxide systems, Acta Mater. 61 (2013) 4374–4383.
[11] M. Parise, O. Sicardy, G. Cailletaud, Modelling of the mechanical behavior of the metal-oxide system during Zr alloy oxidation, J. Nucl. Mater. 256 (1998) 35–46.
[12] F.M. Beremin, A. Pineau, F. Mudry, J.-C. Devaux, Y. D'Escatha, P. Ledermann, A local criterion for cleavage fracture of a nuclear pressure vessel steel, Metall. Trans. A 14 (1983) 2277–2287.
[13] A. Ly, A. Ambard, M. Blat-Yrieix, L. Legras, P. Frankel, M. Preuss, et al., Understanding crack formation at the metal/oxide interface during corrosion of Zircaloy-4 using a simple mechanical model, J. ASTM Int. 8 (2011) 1–18.
[14] V.V. Likhanskii, T.N. Aliev, M.Y. Kolesnik, I.A. Evdokimov, V.G. Zborovskii, Method of elastic energy minimization for evaluation of transition parameters in oxidation kinetics of Zr alloys, Corros. Sci. 61 (2012) 143–147.
[15] J.Y. Park, B.K. Choi, S.J. Yoo, Y.H. Jeong, Corrosion and oxide properties of HANA alloys, J. ASTM Int. 5 (2008) 471–485.
[16] Y.Z. Liu, J.Y. Park, H.G. Kim, Y.H. Jeong, Oxide structure and corrosion mechanism of ZrSnNbFeCrCu alloy studied with transmission electron microscopy and nano-indentation: relation to corrosion kinetics, Mater. Chem. Phys. 122 (2010) 408–416.
[17] N. Ni, D. Hudson, J. Wei, P. Wang, S. Lozano-Perez, G.D.W. Smith, et al., How the crystallography and nanoscale chemistry of the metal/oxide interface develops during the aqueous oxidation of zirconium cladding alloys, Acta Mater. 60 (2012) 7132–7149.
[18] H. Anada, K. Nomoto, Y. Shida, Corrosion behavior of zircaloy-4 sheets produced under various hot-rolling and annealing conditions, zirconium in the nuclear industry: 10th international symposium, ASTM STP 1245 (1994) 307–327.
[19] N. Dai, L.C. Zhang, J. Zhang, Q. Chen, M. Wu, Corrosion behaviour of selective laser melted Ti–6Al–4V alloy in NaCl solution, Corros. Sci. 102 (2016) 484–489.
[20] L. Chen, J. Li, Y. Zhang, W. Lu, L.C. Zhang, L. Wang, D. Zhang, Effect of low-temperature pre-deformation on precipitation behavior and microstructure of a Zr–Sn–Nb–Fe–Cu–O alloy during fabrication Di Zhang, J. Nucl. Sci. Technol. (2015), http://dx.doi.org/10.1080/00223131.2015.1059776 (in press).
[21] M.Y. Yao, B.X. Zhou, Q. Li, W.Q. Liu, X. Geng, Y.P. Lu, A superior corrosion behavior of Zircaloy-4 in lithiated water at 360 °C/18.6 MPa by β-quenching, J. Nucl. Mater. 374 (2008) 197–203.
[22] G.P. Sabol, ZIRLO™—an alloy development success, J. ASTM Int. 2 (2005) 3–24.
[23] L. Chai, B. Luan, K.L. Murty, Q. Liu, Effect of predeformation on microstructural evolution of a Zr alloy during 550–700 °C aging after β quenching, Acta Mater. 61 (2013) 3099–3109.
[24] P. Tejland, H.O. Andrén, Origin and effect of lateral cracks in oxide scales formed on zirconium alloys, J. Nucl. Mater. 430 (2012) 64–71.
[25] E. Polatidis, P. Frankel, J. Wei, M. Klaus, R.J. Comstock, A. Ambard, et al., Residual stresses and tetragonal phase fraction characterisation of corrosion tested Zircaloy-4 using energy dispersive synchrotron X-ray diffraction, J. Nucl. Mater. 432 (2013) 102–112.
[26] L.J. Chai, B.F. Luan, S.S. Gao, J.W. Chen, Q. Liu, Study of precipitate evolution and recrystallization of β-quenched Zr–Sn–Nb–Fe–Cr–Cu alloy during aging, J. Nucl. Mater. 427 (2012) 274–281.
[27] M.V. Farahani, E. Emadoddin, M. Emamy, A.H. Raouf, Effect of grain refinement on mechanical properties and sliding wear resistance of extruded Sc-free 7042 aluminum alloy, Mater. Des. 54 (2014) 361–367.
[28] L. Saintoyant, L. Legras, Y. Bréchet, Effect of an applied stress on the recrystallization mechanisms of a zirconium alloy, Scr. Mater. 64 (2011) 418–421.
[29] J. Wei, P. Frankel, E. Polatidis, M. Blat, A. Ambard, R.J. Comstock, et al., The effect of Sn on autoclave corrosion performance and corrosion mechanisms in Zr–Sn–Nb alloys, Acta Mater. 61 (2013) 4200–4214.
[30] J.H. Lee, S.K. Hwang, Effect of Mo addition on the corrosion resistance of Zr-based alloy in water containing LiOH, J. Nucl. Mater. 321 (2003) 238–248.
[31] W. Gong, H. Zhang, Y. Qiao, H. Tian, X. Ni, Z. Li, et al., Grain morphology and crystal structure of pre-transition oxides formed on Zircaloy-4, Corros. Sci. 74 (2013) 323–331.
[32] W. Gong, H. Zhang, C. Wu, H. Tian, X. Wang, The role of alloying elements in the initiation of nanoscale porosity in oxide films formed on zirconium alloys, Corros. Sci. 77 (2013) 391–396.
[33] C. Proff, S. Abolhassani, C. Lemaignan, Oxidation behaviour of zirconium alloys and their precipitates — a mechanistic study, J. Nucl. Mater. 432 (2013) 222–238.
[34] W. Qin, C. Nam, H.L. Li, J.A. Szpunar, Tetragonal phase stability in $ZrO_2$ film formed on zirconium alloys and its effects on corrosion resistance, Acta Mater. 55 (2007) 1695–1701.
[35] A. Lyapin, L.P.H. Jeurgens, E.J. Mittemeijer, Effect of temperature on the initial, thermal oxidation of zirconium, Acta Mater. 53 (2005) 2925–2935.
[36] I.G. Ritchie, A. Atrens, The diffusion of oxygen in alpha-zirconium, J. Nucl. Mater. 67 (1977) 254–264.
[37] M. Kiran Kumar, C. Vanitha, I. Samajdar, G.K. Dey, R. Tewari, D. Srivastava, et al., Deformation texture and microtexture developments in a cold rolled single phase hexagonal Zircaloy 2, Mater. Sci. Technol. 22 (2006) 331–342.
[38] Y. Amouyal, S.V. Divinski, L. Klinger, E. Rabkin, Grain boundary diffusion and recrystallization in ultrafine grain copper produced by equal channel angular pressing, Acta Mater. 56 (2008) 5500–5513.
[39] V. Likhanskii, M. Kolesnik, On the evolution of wave structure at the metal/oxide interface during oxidation of Zr alloys, Corros. Sci. 87 (2014) 416–420.